RSC Advances

PAPER

View Article Online
View Journal | View Issue

Check for updates

Cite this: *RSC Adv.*, 2025, **15**, 39630

Semimetallic superconductivity in cubic Nd_3In: a first-principles insight into indium-based compounds

Arafat Rahman, Alamgir Kabir * and Tareq Mahmud

The quest for materials that simultaneously exhibit superconductivity and nontrivial topology has drawn significant attention in recent years, driven by their potential to host exotic quantum states. Their unique coexistence often leads to rich physics and potential applications in quantum technologies. Here, we predict cubic Nd_3In as an exceptional candidate in this class, combining strong-coupling superconductivity with distinctive topological features. Using first-principles calculations, we find that the strong-coupling superconductivity in Nd_3In arises primarily due to pronounced Fermi surface nesting, leading to an electron–phonon coupling constant of $\lambda = 1.39$. Our fully anisotropic Migdal–Eliashberg analysis predicts a superconducting transition temperature $T_c \approx 14$ K at ambient pressure, which is the highest value reported so far among cubic semimetallic superconductors. When subjected to a pressure of 15 GPa, T_c increases further to 18 K. Beyond superconductivity, Nd_3In is found to be a Weyl semimetal, as evidenced by the presence of Fermi arcs and nontrivial Z_2 topological invariants, confirming its topological nature. The combination of strong-coupling superconductivity and nontrivial topological states makes Nd_3In a promising candidate for quantum transport and topological quantum computation.

Received 5th August 2025
Accepted 9th October 2025

DOI: 10.1039/d5ra05713b

rsc.li/rsc-advances

Open Access Article. Published on 21 October 2025. Downloaded on 12/23/2025 3:16:47 AM.
This article is licensed under a Creative Commons Attribution-NonCommercial 3.0 Unported Licence.

1. Introduction

Semimetallic superconductors lie at the forefront of condensed matter physics, where the interplay between topological states and electron–phonon interactions gives rise to novel quantum phenomena.[1–10] These superconductors not only host Majorana fermions which are crucial for quantum information technologies and topological quantum computation protected from decoherence[11–21] but also give rise to a variety of intriguing quantum phenomena, including topological quantum spin liquids,[22–24] the quantum Hall effect,[25–28] quantum transport,[29–31] and potential applications in high-speed electronics.[32] Both layered and bulk materials have been found to host semimetallic superconductivity, expanding the landscape for exploring exotic quantum phases.[33–39] Among layered materials, W_2N_3 stands out with a predicted superconducting transition temperature T_c of 21–28 K, which is one of the highest reported in semimetallic systems.[40] Unlike layered materials, bulk compounds such as $AuCu_3$-type intermetallics are known for their simple cubic symmetry and the versatility of their intriguing properties, such as magnetic ordering,[41] heavy fermion behavior,[42,43] topological characteristics[44–46] and superconductivity.[47–49] Beyond superconductivity, many $AuCu_3$-type intermetallics also display topological superconductivity.

For instance, Sn_3Ca ($T_c = 4.2$ K), a superconducting semimetal[50] known for its potential in quantum computing,[51] whereas Sn_3Y ($T_c = 7$ K) hosts nontrivial band topology,[52,53] and Sn_3La ($T_c = 5.9$–6.3 K) displays similar traits under applied pressure.[54] Additionally, the Tl_3Y and Pb_3Y compounds exhibit Rashba-like surface states and phonon-mediated superconductivity, with transition temperatures of $T_c = 4.37$ K and 2.17 K, respectively.[53] These low T_c superconductors have become integral to technologies such as fusion reactors, particle accelerators, magnetic resonance imaging (MRI), and superconducting radio frequency (SRF) cavities.[55] For example, Nb_3Sn, with a transition temperature of $T_c = 18.3$ K,[56] is widely utilized in the aforementioned; technologies.[57–60] Moreover, recent experiments have been able to detect the presence of topologically protected surface states in superconductors, including the observation of chiral surface states[61–63] and Fermi arcs in semimetallic systems.[64,65] These discoveries have significantly advanced the field, expanding the frontier of both fundamental physics and practical applications.

Despite Indium (In) being a well-known elemental superconductor, research on In-based superconducting compounds has remained limited. Most available studies were conducted several decades ago and include compounds such as La_3In ($T_c = 9.5$ K),[66] In_3Ce ($T_c = 0.2$ K),[67] InHg ($T_c = 3.1$–4.5 K),[68] InSn ($T_c = 3.4$–6.6 K),[69] InTl ($T_c = 2.5$–3.8 K),[70] and InSb ($T_c = 1.88$ K).[71] This lack of recent investigation reveals a significant gap in the study of In-based superconductors, especially in the context of modern materials discovery. Furthermore it has been observed

Department of Physics, University of Dhaka, Dhaka 1000, Bangladesh. E-mail: alamgir.kabir@du.ac.bd; tareqphy1205@gmail.com

© 2025 The Author(s). Published by the Royal Society of Chemistry

Open Access Article. Published on 21 October 2025. Downloaded on 12/23/2025 3:16:47 AM. This article is licensed under a Creative Commons Attribution-NonCommercial 3.0 Unported Licence.

that rare earth substitutions particularly involving Neodymium (Nd) have demonstrated notable success in enhancing T_c across various systems.[72–74] This suggests that the unique combination of In and Nd in Nd_3In could provide a promising route for improving superconducting properties. Moreover, X-ray diffraction analysis indicates that Nd_3In crystallizes in a cubic structure,[75] aligning it structurally with the class of previously discussed AuCu3-type cubic superconductors. The presence of heavy atoms such as Nd and In in Nd_3In is expected to produce strong spin–orbit coupling effects that significantly influence its electronic structure and give rise to topological phases, while also enabling spintronic applications.[76] Exploring the superconducting and topological aspects of Nd_3In not only revives interest in In-based superconductors but also contributes to the broader search for high-performance semimetallic superconductors within the AuCu3-type family. In this study, we present a comprehensive theoretical investigation of the electronic, phononic, superconducting, and topological properties of cubic Nd_3In. The study begins with the analysis of the electronic structure including spin–orbit coupling in Section 3.1, followed by phonon calculations to investigate lattice dynamics and possible soft modes in Section 3.2. In Section 3.3, we evaluate the Fermi surface nesting and electron–phonon coupling to uncover the microscopic origin of superconductivity in Nd_3In. Finally, Section 3.4 is devoted to exploring its topological characteristics.

2. Methodology and crystal structure

The crystal structure of Nd_3In belongs to the primitive cubic space group $Pm\bar{3}m$ (No. 221), with a calculated lattice parameter of 4.977 Å (4.982 Å with SOC), which are in close agreement with the experimentally reported value.[75,77] In this structure, the In atom occupies the high-symmetry 1a Wyckoff position at the origin (0.0, 0.0, 0.0), while the Nd atoms are located at the 3c Wyckoff positions with fractional coordinates (0.0, 0.5, 0.5), (0.5, 0.0, 0.5), and (0.5, 0.5, 0.0). The optimized crystal structure of Nd_3In and its corresponding Brillouin zone are illustrated in Fig. 1(a) and (b), respectively.

First-principles calculations based on density functional theory (DFT) are performed using the plane-wave pseudopotential code Quantum ESPRESSO.[78] The exchange-correlation potential is treated within the generalized gradient approximation (GGA) using the Perdew–Burke–Ernzerhof (PBE) functional. Scalar-relativistic ultrasoft pseudopotentials are used for both Nd and In atoms. For Nd, the 4f electrons are strongly localized and therefore excluded from the valence states. They are treated as frozen core states following the standard open-core approach, since conventional DFT does not provide a reliable description of localized f electrons.[79–81] The valence electron configurations considered are 4d, 5s, and 5p for In, and 5d, 6s, and 6p for Nd. A kinetic energy cutoff of 75 Ry is used for the plane-wave basis set, with a charge density cutoff of 350 Ry. The Brillouin zone is sampled using a Γ-centered $24 \times 24 \times 24$ k-mesh. Gaussian smearing with a width of 0.0125 Ry is applied for electronic occupations. Structural relaxations are carried out until the total energy and atomic forces converge below 1.0×10^{-10} Ry and 1.0×10^{-6} Ry per Bohr, respectively. Phonon dispersions, electron–phonon interactions, and superconducting parameters are evaluated using density functional perturbation theory (DFPT). For accurate estimation of superconducting properties, the EPW package is employed, which uses Wannier interpolation of electron–phonon matrix elements to efficiently calculate key quantities on dense grids.[82] It should be noted that EPW cannot be applied within DFT + U calculations, which are often required for localized f systems. Furthermore, the use of hybrid functionals would improve the electronic description but is computationally expensive and beyond the scope of this study. The superconducting transition temperature T_c is estimated using the Allen–Dynes modification of the McMillan formula:[83]

$$T_c = f_1 f_2 \frac{\omega_{\log}}{1.2} \exp\left[\frac{-1.04(1+\lambda)}{\lambda - \mu^*(1+0.62\lambda)}\right] \quad (1)$$

where $\omega_{\log}$ denotes the logarithmic average of phonon frequencies, and μ^* is the retarded Coulomb pseudopotential. The correction factors f_1 and f_2 are expressed as

$$f_1 f_2 = \left[1 + \left(\frac{\lambda}{2.46(1+3.8\mu^*)}\right)^{\frac{3}{2}}\right]^{\frac{1}{3}} \times \left(1 - \frac{\lambda^2\left(1 - \frac{\omega_2}{\omega_{\log}}\right)}{\lambda^2 + 3.312(1+6.3\mu^*)^2}\right) \quad (2)$$

With ω_2 being the mean-square phonon frequency defined by

$$\omega_2 = \left[\frac{1}{\lambda}\int_0^{\omega_{\max}} \frac{2\alpha^2F(\omega)}{\omega}\omega^2 d\omega\right]^{1/2} \quad (3)$$

The total electron–phonon coupling (EPC) constant λ is given by

$$\lambda = 2\int_0^{\infty} \frac{\alpha^2F(\omega)}{\omega} d\omega \quad (4)$$

where $\alpha^2F(\omega)$ is the Eliashberg spectral function, defined as.

$$\alpha^2F(\omega) = \frac{1}{N_F}\sum_{\boldsymbol{q},\nu}\sum_{mn\boldsymbol{k}} |g_{mn}{}^{\nu}(\boldsymbol{k},\boldsymbol{q})|^2 \delta(\varepsilon_{m\boldsymbol{k}} - \varepsilon_F) \times \delta(\varepsilon_{n,\boldsymbol{k}+\boldsymbol{q}} - \varepsilon_F)\delta(\omega - \omega_{\nu\boldsymbol{q}}) \quad (5)$$

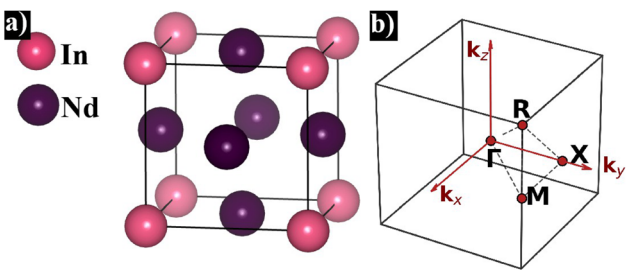

Fig. 1 (a) Crystal structure and (b) Brillouin zone of Nd_3In.

Open Access Article. Published on 21 October 2025. Downloaded on 12/23/2025 3:16:47 AM. This article is licensed under a Creative Commons Attribution-NonCommercial 3.0 Unported Licence.

Here, $g^{\nu}_{mn}(\boldsymbol{k},\boldsymbol{q})$ are the electron–phonon matrix elements, and $\omega_{\nu\boldsymbol{q}}$ are the phonon frequencies. To further investigate the electronic structure, the Fermi surface nesting function $\zeta(\boldsymbol{q})$ is computed as

$$\xi(\boldsymbol{q}) = \frac{1}{\Omega_{\mathrm{BZ}}}\int_{\mathrm{BZ}} \mathrm{d}\boldsymbol{k}\sum_{m,n}\delta(\varepsilon_{n\boldsymbol{k}} - \varepsilon_F) \times \delta\left(\varepsilon_{m,\boldsymbol{k}+\boldsymbol{q}} - \varepsilon_F\right) \quad (6)$$

where Ω_{BZ} is the Brillouin zone volume and ϵ_F is the Fermi energy. Topological properties, including surface states and invariants, are computed using WANNIER90 (ref. 84) and WANNIERTOOLS.[85] Maximally localized Wannier functions are constructed with spin–orbit coupling (SOC), and surface Green's function methods are used to resolve the surface band structure. Topological invariants are evaluated from the Wannier-based tight-binding model.

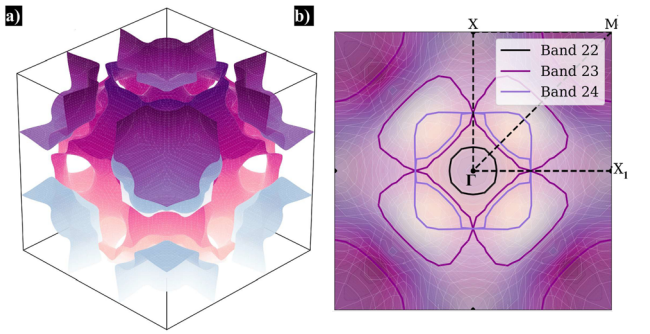

Fig. 3 (a) Fermi surface in reciprocal space. (b) Contours of the Fermi surface on the $k_z = 0$ plane, with dashed lines indicating the high symmetry points.

3. Results and discussion

3.1. Electronic properties

The orbital projected band structure of Nd_3In (without SOC), along with its DOS is shown in Fig. 2. As shown in the right panel of Fig. 2, the Nd d states dominate the electronic structure across the entire energy range. Notably, the primary contribution at the Fermi level comes from the Nd d_z^2 orbitals, followed by the d_{zx}, d_{zy} and Nd p orbitals, as these are the most saturated near the Fermi energy. The left panel of Fig. 2 illustrates bands 22, 23, and 24 intersect the Fermi level, resulting in the formation of three distinct Fermi surfaces, all displayed together in a single plot in Fig. 3(a). The Fermi surface arising from band 22 forms a hole pocket around the Γ point, primarily composed of Nd p orbital character and outlined by the black contour as illustrated in Fig. 3(b). Band 23 gives rise to hole-like pockets near the M point and four electron-like pockets along the M–Γ direction, as indicated by the purple contours in Fig. 3(b). These hole pockets near the M point can be explicitly seen in Fig. 3(a). These features predominately originate from Nd d_{zx} and d_{z^2} orbitals. Lastly, band 24 forms a nearly rectangular electron-like pocket, indicated by the medium purple

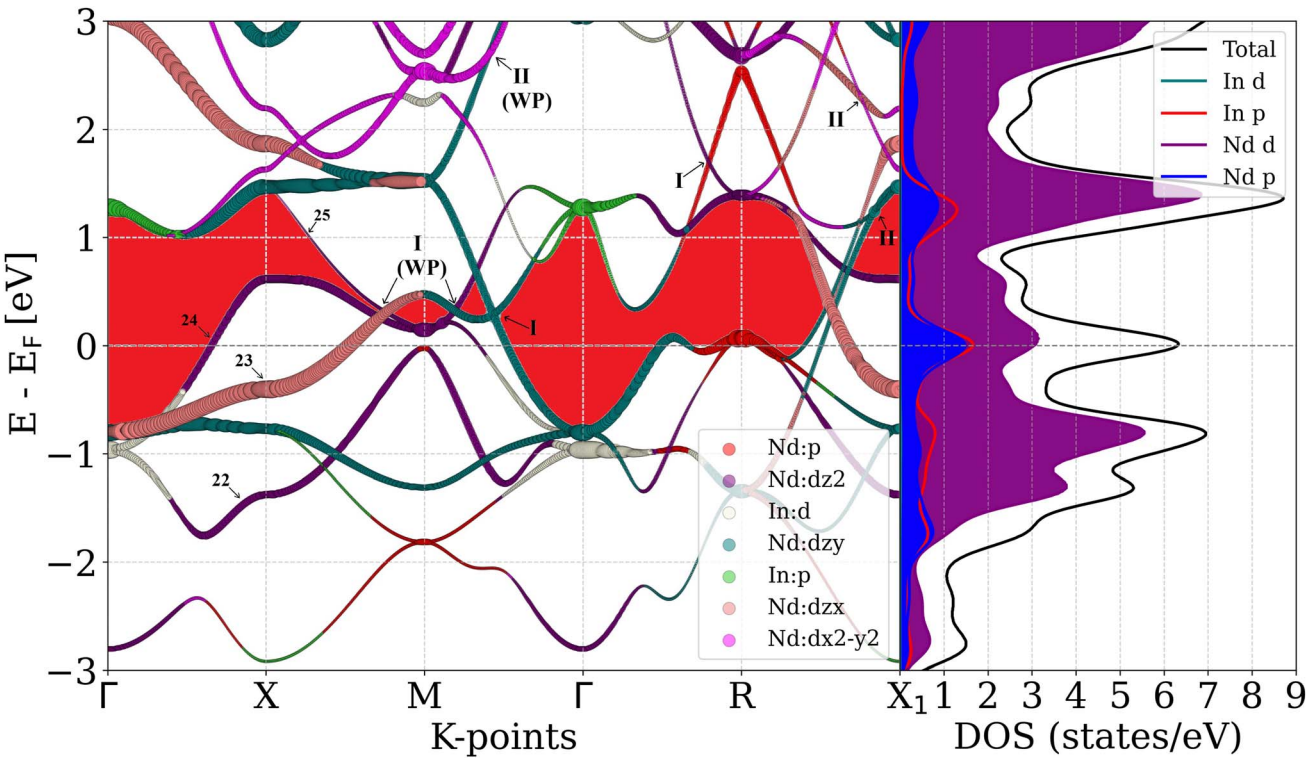

Fig. 2 Orbital projected electronic band structure and corresponding density of states (DOS) for Nd_3In. The Fermi energy (EF) is set to zero and indicated by the dashed horizontal line. The size of the colored scatter points is proportional to the contribution from the selected atomic orbitals. Several Weyl points are observed in the band structure, among which a few representative points are highlighted. The red-shaded region in the left panel marks the locations of type-I Weyl points, which occur between bands 24 and 25.

© 2025 The Author(s). Published by the Royal Society of Chemistry

Open Access Article. Published on 21 October 2025. Downloaded on 12/23/2025 3:16:47 AM. This article is licensed under a Creative Commons Attribution-NonCommercial 3.0 Unported Licence.

contours in Fig. 3(b), primarily originating from the Nd d_{z^2} orbital. Within this rectangular pocket, four smaller hole pockets are embedded, which stem from the Nd d_{z^2}, d_{zy} and p orbitals. A particularly striking characteristic of the Fermi surface is the presence of several nearly parallel segments, indicating strong Fermi surface nesting, which leads to strong electron–phonon interaction.[86–88] The nesting vectors can be identified along the Γ–X, Γ–M, and Γ–X_1 directions, connecting flat regions of the Fermi surface. Upon the inclusion of spin–orbit coupling (SOC), six bands (indexed 43 to 48) are observed to cross the Fermi level, with three of them being pairwise degenerate, as illustrated in Fig. 4(a). The corresponding density of states at the Fermi level, N (EF), shows a slight decrease from approximately 6.192 eV (without SOC) to 6.118 eV, as presented in Fig. 4(b), indicating that SOC has a minimal effect on the overall electronic density of states in Nd_3In. However, SOC significantly affects the band structure of Nd_3In by lifting degeneracies and opening finite energy gaps as shown in Fig. 4(c). The bulk band structure without SOC hosts several Weyl points of both type-I and type-II, a few of which are marked in Fig. 2. Type-I Weyl points correspond to band crossings that produce point-like Fermi surfaces, whereas type-II Weyl points occur at the intersection between electron and hole pockets, giving rise to significantly tilted Weyl cones.[76,89–91] When SOC is included, a number of these Weyl crossings are lifted, modifying the bulk electronic spectrum. This effect can be clearly seen in Fig. 4(c). In the case without SOC, three band-touching points appear within the plotted energy range, dividing the spectrum into four distinct regions labeled I–IV. These touching points prevent the opening of a global gap and give rise to apparent partial-gap features. Upon inclusion of SOC, two of these Weyl points are annihilated due to SOC induced splitting, leaving only a single Weyl point between regions I and II. As a result, the spectrum reorganizes into two main regions, and although partial gaps are present, no full insulating gap opens. The persistence of this Weyl point ensures that Nd_3In retains its semimetallic character under SOC rather than becoming a topological insulator. This behavior is consistent with previous reports on SOC in topological semimetals, where SOC often eliminates some Weyl nodes but leaves others intact, thereby stabilizing the Weyl semimetal phase.[92] Additionally, the SOC band structure exhibits double degeneracy throughout the Brillouin zone, indicative of Kramers degeneracy.[93] This degeneracy indicates the preservation of time-reversal symmetry (TRS) in the system and suggests the possibility of nontrivial topological properties.[94] These observations indicate the presence of nontrivial topological states in Nd_3In, the detailed analysis of which is presented in Section 3.4. Furthermore, SOC also alters the orbital character and the topology of the Fermi surfaces. The dominant states now arise form the Nd $d_{x^2-y^2}$, d_{zx}, and d_{z^2} orbitals, with a noticeable increase in the contribution from In p orbitals, which previously played a minimal role in the non-SOC case. The Fermi surfaces corresponding to the three non-degenerate bands (bands 44, 46 and 48) are shown in Fig. 5(a), while their degenerate partners (bands 43, 45, and 47) exhibit identical features and are therefore not shown separately. Without SOC, the Fermi surface features a prominent rectangular electron-like contour, primarily originating from band 24. After incorporating SOC, this contour disappears and is replaced by lobed teal-colored contours shown in Fig. 5(b). This change arises because bands 46 and 48, which correspond to bands 23 and 24 in the absence of SOC, become non-degenerate near the Fermi level along the Γ–R and R–M directions. These bands now cross the

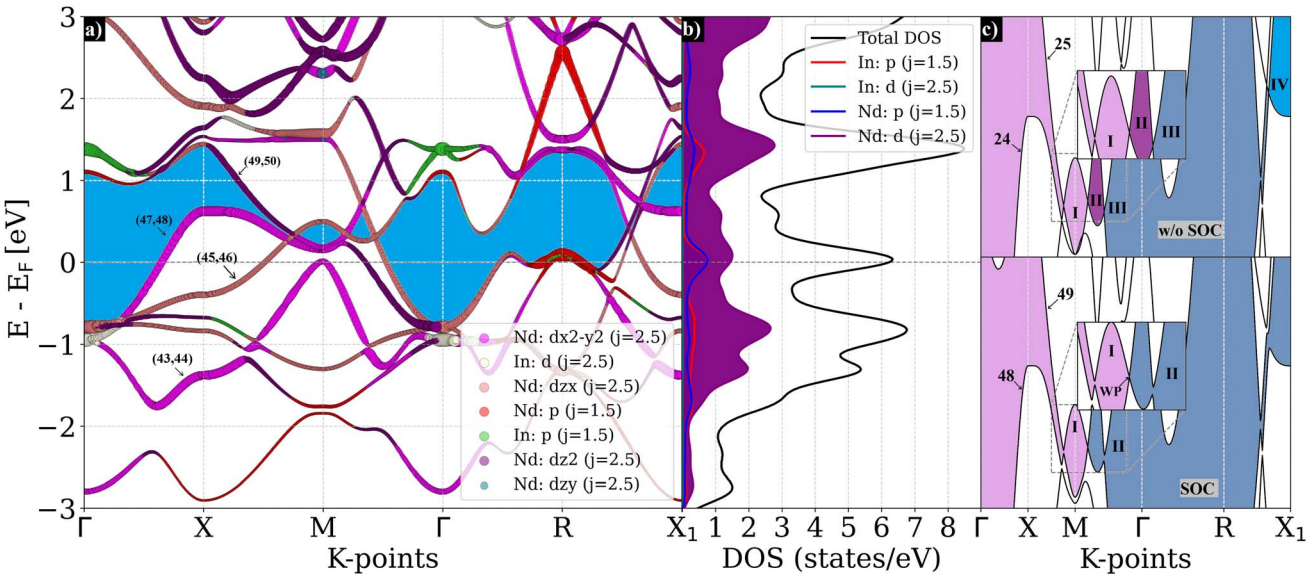

Fig. 4 (a) SOC-induced orbital-projected electronic band structure of Nd_3In and (b) the corresponding density of states (DOS). The Fermi energy (EF) is set to zero and indicated by the dashed horizontal line. The size of the colored scatter points in panel (a) reflects the relative contribution of the selected atomic orbitals. (c) Effect of SOC on the band structure. Without SOC (upper inset), three band-touching points divide the spectrum into four regions (I–IV). Inclusion of SOC (lower inset) lifts two of these nodal points, leaving a single Weyl point and partially gapped regions.

Open Access Article. Published on 21 October 2025. Downloaded on 12/23/2025 3:16:47 AM. This article is licensed under a Creative Commons Attribution-NonCommercial 3.0 Unported Licence.

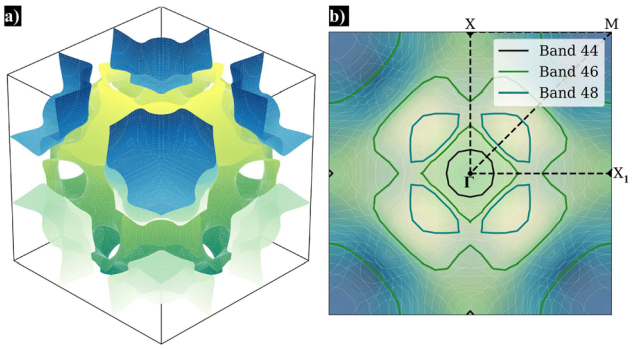

Fig. 5 (a) Fermi surface including spin–orbit coupling (SOC) displayed in reciprocal space. (b) Cross-sectional contours of the Fermi surface on the $k_z = 0$ plane, where dashed lines denote high-symmetry points.

Fermi level at different k-points, altering the Fermi surface topology.

3.2. Phonon dispersion and electron–phonon interaction

The phonon dispersion and projected phonon density of states (PHDOS) for cubic Nd_3In are shown in Fig. 6(a) and (b). The absence of imaginary frequencies throughout the Brillouin zone confirms the dynamical stability of the structure. The phonon spectrum of Nd_3In can be divided into three distinct frequency regions. This distribution reflects the expected behavior that heavier atoms like Nd vibrate at lower frequencies than lighter atoms such as In. A closer inspection of the phonon dispersion reveals the presence of soft phonon modes, or Kohn anomalies, along specific high-symmetry directions particularly along the Γ–X–M and R–X paths. Generally, these soft phonon modes are indicative of strong electron-phonon coupling.[95–98]

All the three acoustic branches, as shown in Fig. 6(a), exhibit noticeable softening along these directions, with the sixth vibrational mode showing pronounced softening along R–X_1. We have also examined the pressure dependence of this phonon softening, as shown in Fig. S1 of SI Materials.[99]

The phonon dispersion weighted by mode-resolved electron–phonon coupling strength and the corresponding spectral functions were computed at 10 GPa and 15 GPa pressure. The softening intensifies under applied pressure, suggesting a possible enhancement in the superconducting critical temperature. Fig. 6(c) shows the Eliashberg spectral function $\alpha^2F(\omega)$ and the cumulative EPC function $\lambda(\omega)$.

To understand the microscopic origin of the strong electron–phonon coupling, we analyzed the phonon eigenvectors of the most strongly coupled modes. Two representative modes with the highest EPC values (λ_{qv}) are highlighted in Fig. 6(a). The phonon mode at the X point (Mode 1, $\approx$ 45 cm^{-1}) is dominated by the vibrations of two Nd atoms oscillating in opposite directions, while the remaining atoms remain stationary as illustrated in Fig. 6(d). The next strongly coupled mode (Mode 2, $\approx$ 65 cm^{-1}), also located at the X point, involves one Nd atom and In atom vibrating out of phase with unequal amplitudes, while the other atoms remain immobile as shown in Fig. 6(e). This specific relative motion of the atoms strongly perturbs the electronic states near the Fermi energy, accounting for its significant role in the EPC.

To investigate the origin of the Kohn anomalies at ambient pressure, we computed the Fermi surface nesting function $\zeta(\mathbf{Q})$ using the EPW code on a dense k-grid of 64 × 64 × 64 and a q-grid of 32 × 32 × 32, as shown in Fig. 7. The nesting function

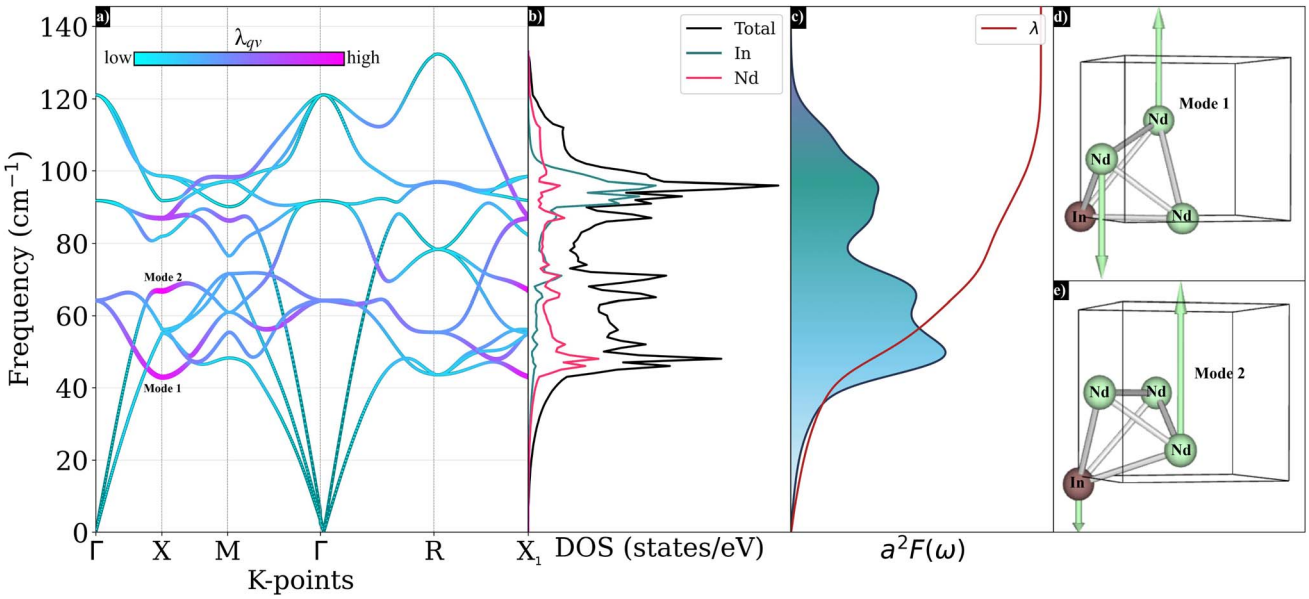

Fig. 6 (a) Phonon dispersion relations weighted by the mode-resolved electron–phonon coupling strength λ_{qv}, where magenta shading indicates stronger coupling and cyan shading denotes weaker coupling. (b) Atom-projected phonon density of states (PHDOS). (c) Eliashberg spectral function $\alpha^2F(\omega)$ and cumulative electron–phonon coupling constant $\lambda(\omega)$ as functions of phonon frequency. (d–e) Visualization of the two dominant phonon modes contributing most strongly to the EPC.

© 2025 The Author(s). Published by the Royal Society of Chemistry

Open Access Article. Published on 21 October 2025. Downloaded on 12/23/2025 3:16:47 AM.
This article is licensed under a Creative Commons Attribution-NonCommercial 3.0 Unported Licence.

exhibits pronounced peaks along high-symmetry directions where phonon softening is observed, indicating strong Fermi surface nesting. At the Γ point, the prominent peak corresponds to the entire Fermi surface nesting onto itself, which lacks physical significance. Fig. 7 shows that $\zeta(\mathbf{Q})$ exhibits notably high values along the $\Gamma \rightarrow X$, $\Gamma \rightarrow X_1$ directions and as well as between the $\Gamma \rightarrow M$ path. As previously discussed, this indicates that parallel segments of the Fermi surface are connected by specific wave vectors **Q**, in accordance with the features observed in the calculated Fermi surfaces shown in Fig. 3(b). Such nesting enhances the electron–phonon interaction, leading to strong-coupling and giving rise to Kohn anomalies.[87,100–103] We then performed a quantitative evaluation of the electron–phonon coupling (EPC) strength. Initially, density-functional perturbation theory (DFPT) calculations on a coarse $4 \times 4 \times 4$ **q**-mesh yielded a preliminary EPC constant of $\lambda = 0.982$. To obtain a more accurate value, we employed the EPW code, which utilizes maximally localized Wannier functions (MLWFs) to interpolate the electron–phonon matrix elements over dense Brillouin zone grids, specifically a $48 \times 48 \times 48$ ***k***-mesh and a $24 \times 24 \times 24$ **q**-mesh. To construct the MLWFs, we used initial projections on the Nd d and In p orbitals. The accuracy of the Wannierization was verified by comparing the Wannier interpolated band structure with the original DFT results, as shown in Fig. S2 (see SI Materials[99]).

From the EPW calculations, we obtained a refined electron–phonon coupling (EPC) constant of $\lambda = 1.394$, indicating strong coupling and suggesting that Nd_3In is a promising candidate for phonon-mediated superconductivity. The dominant contributions to the total EPC arise from soft phonon modes, as illustrated in Fig. 6 (a), where the mode-resolved coupling strengths $\lambda_{q\nu}$ are projected onto the phonon dispersion. A pronounced enhancement of $\lambda_{q\nu}$ is observed along the Γ–X–M and R–X_1 directions, which coincide with regions of phonon softening. Analysis of $\lambda(\omega)$ reveals that phonons below 65 cm^{-1} contribute approximately 62.1% of the total EPC, while intermediate-frequency modes between 65 and 90 cm^{-1} account for 20.8%. The remaining contribution comes from higher-frequency modes.

3.3. Superconductivity

To investigate the superconducting behavior of cubic Nd_3In, we begin by examining the nature of its superconducting gap and the strength of electron–phonon interactions. Our analysis reveals that Nd_3In exhibits a single-gap superconducting state across the Fermi surface, as shown in Fig. 8(a). This one gap nature is further supported by a single, sharp peak in the superconducting quasiparticle density of states (QDOS) at different temperatures, illustrated in Fig. 8(b). Tunneling spectroscopy experiments can directly probe this

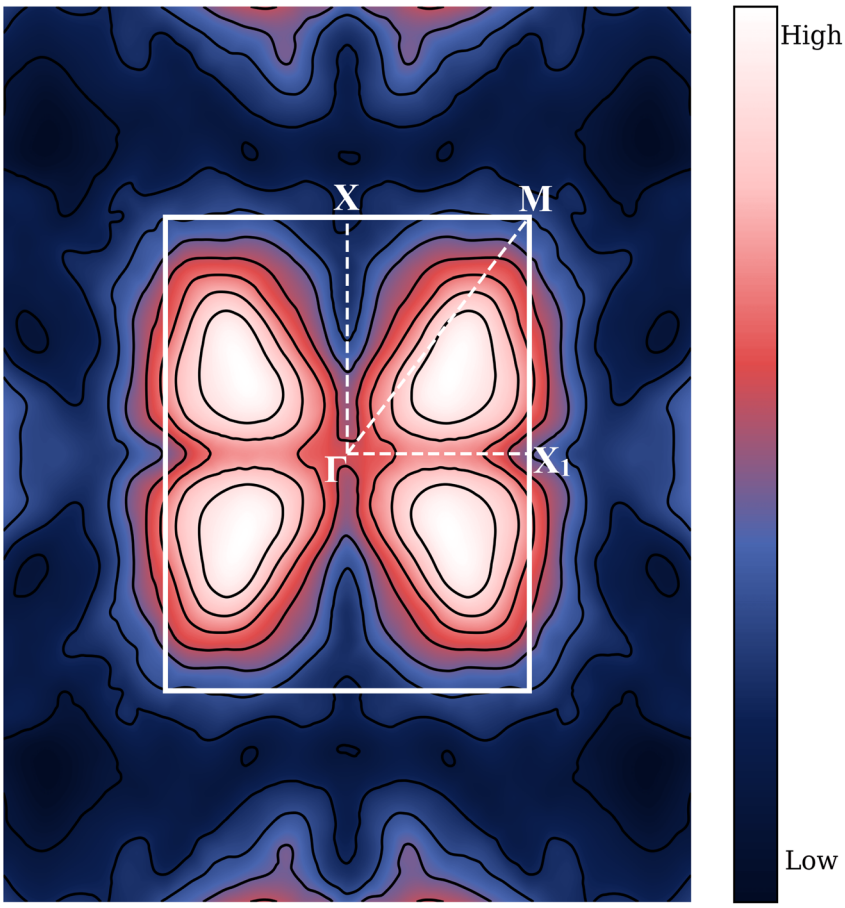

Fig. 7 The Fermi surface nesting function $\zeta(\vec{Q})$ in the $k_z = 0$ plane of Nd_3In. SOC is not considered.

Open Access Article. Published on 21 October 2025. Downloaded on 12/23/2025 3:16:47 AM. This article is licensed under a Creative Commons Attribution-NonCommercial 3.0 Unported Licence.

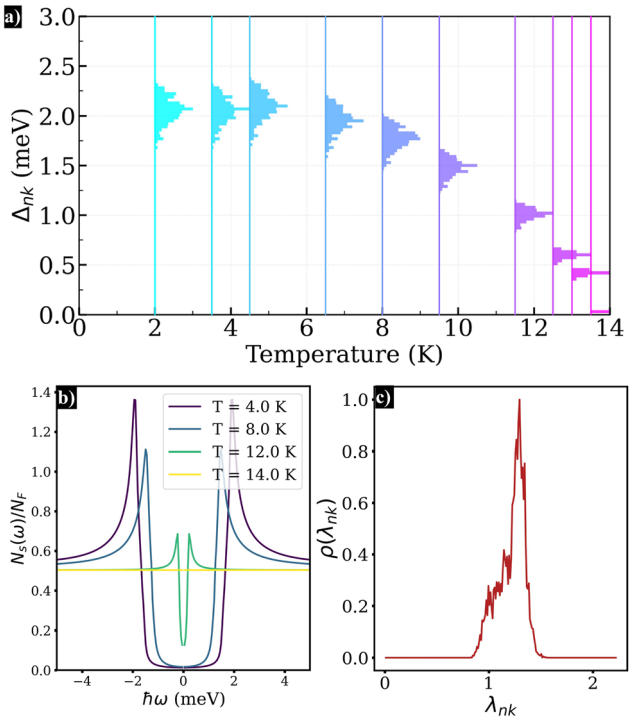

Fig. 8 (a) Energy distribution of the anisotropic superconducting gap as a function of temperature. (b) The quasiparticle density of states (DOS) in the superconducting state compared to the normal-state DOS as a function of energy. The superconducting DOS has been rescaled to maT_ch the normal-state DOS, allowing easy comparison with experiments. (c) The distribution of anisotropic electron phonon coupling (EPC) strength λ_k, showing a wide variation due to strong anisotropy.

superconducting QDOS.[104] Typically, an *s*-wave superconductor shows a U-shaped QDOS, while a d-wave superconductor exhibits a V-shaped profile.[105] Our calculated QDOS clearly displays a U-shaped signature, reflecting conventional s-wave pairing symmetry in Nd_3In. The electron–phonon coupling (EPC) coefficient in Nd_3In exceeds 1.3, indicating a strong-coupling regime. In such cases, the full Allen–Dynes formula is typically employed to estimate the superconducting transition temperature.[100] Using the widely accepted Coulomb pseudopotential value of $\mu^* = 0.1$,[106–108] this approach yields a predicted T_c of 9.498 K. However, the Allen-Dynes formula does not account for the momentum dependence of the electron–phonon interaction across the Fermi surface and therefore fails to accurately describe materials exhibiting significant anisotropy.[109] To better capture the anisotropic nature of EPC in Nd_3In, we analyze the momentum-dependent EPC strength, defined as $\lambda_{k'} = \sum_{k'} W_{k'} \lambda(\boldsymbol{k}, \boldsymbol{k}', n = 0)$. As shown in Fig. 8(c), the λ_k values span a wide range from 0.85 to 1.57, clearly indicating strong anisotropy and underscoring the limitations of isotropic approximation in this system. To obtain a more reliable estimate of the superconducting critical temperature T_c, we employ fully anisotropic Migda–Eliashberg calculations, which explicitly incorporate momentum-dependent electron phonon interactions across the Fermi surface.[87,110,111] The temperature evolution of the superconducting energy gap Δ_{nk} is presented in Fig. 8(a). At 2 K, the gap ranges from 1.75 to 2.30 meV, reflecting its anisotropic nature. As temperature increases, the gap gradually closes and disappears around 14 K, which we identify as the true superconducting transition temperature. This value shows a 32.16% enhancement over the isotropic Allen–Dynes estimate, highlighting the significance of momentum-dependent electron–phonon coupling considered in the fully anisotropic Migdal–Eliashberg formalism, as previously mentioned. Notably, Nd_3In exhibits the highest superconducting transition temperature among the $AuCu_3$-type semimetallic superconductors.

Moreover, T_c further increases under pressure, reaching 16.5 K at 10 GPa and 18 K at 15 GPa, as shown in Fig. S3 and S4 (in SI Materials[99]). Thus, Nd_3In can be classified as a low-T_c superconductor and, as previously discussed, holds strong potential for applications in technologies such as MRI, SRF cavities, fusion reactors, and particle accelerators. Furthermore, the ratio $2\Delta_0/k_BT_c = 3.93$ exceeds the BCS weak coupling limit of 3.52, underscoring the strong-coupling character of superconductivity in Nd_3In, which primarily originates from the pronounced Fermi surface nesting. These findings clearly demonstrate that the isotropic McMillan-Allen–Dynes approach underestimates T_c in materials with pronounced EPC anisotropy, while the anisotropic Migdal–Eliashberg theory provides a more robust and detailed understanding of the superconducting mechanism.

3.4. Semimetallic topology

As previously discussed, the SOC-induced electronic band structure of Nd_3In suggests the presence of non-trivial topological behavior, likely arising from time-reversal symmetry (TRS). As shown in Fig. 9, the three-dimensional band structure reveals a linear crossing near the Γ–M path within the energy range of 0.10–0.25 eV, indicating the existence of a type-I Weyl point formed between the lowest conduction band and the highest valence band. Our primary focus remains on this particular crossing, which emerges in close proximity to the Fermi level. Additionally, several other Weyl points of both type-I and type-II appear at higher energies, as shown in Fig. 2. However, these states lie far above the Fermi level and are therefore not discussed here, as they are unlikely to influence the transport properties significantly. To explore the topological characteristics of the type-I Weyl point near the Fermi level, we performed a detailed analysis combining Wannier-based and symmetry-based topological indicators. The initial step involves constructing a tight-binding Hamiltonian using maximally localized Wannier functions (MLWFs), derived from the first-principles calculations. The orbital analysis confirms that bands near the Fermi level are mainly derived from Nd d orbitals. Our self-consistent field (SCF) calculations show that the total magnetization of the system converges to zero, confirming a nonmagnetic ground state for Nd_3In. To ensure that this phase is indeed the most stable, we explicitly considered ferromagnetic (FM), antiferromagnetic (AFM), and nonmagnetic (NM) configurations. The total energies of these

© 2025 The Author(s). Published by the Royal Society of Chemistry

Open Access Article. Published on 21 October 2025. Downloaded on 12/23/2025 3:16:47 AM. This article is licensed under a Creative Commons Attribution-NonCommercial 3.0 Unported Licence.

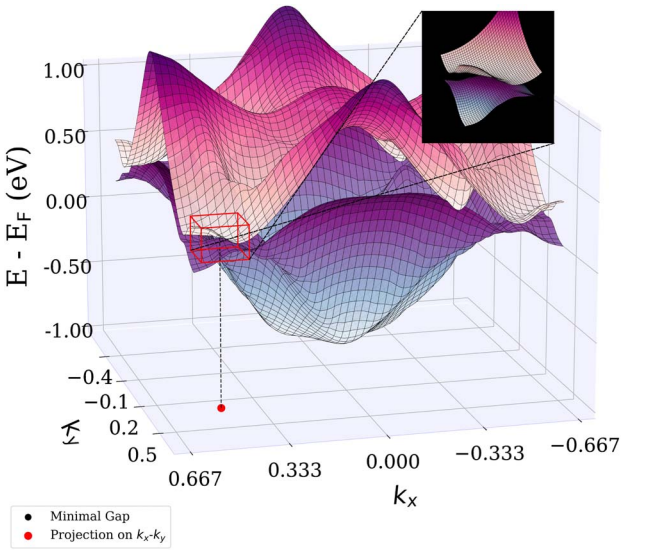

Fig. 9 3D plot of the electronic band structure (with SOC) showing the Weyl point located between the topmost valence and lowest conduction bands. The projection of the Weyl point onto the k_x–k_y plane is marked with a red dot.

configurations are summarized in Table A1 in the SI. The combination of zero magnetization and preserved time-reversal symmetry (TRS) motivates the calculation of Z_2 topological invariants to determine the system's topological classification.[112] These invariants are computed between bands 48 and 49 using the evolution of Wannier charge centers (WCCs),[113,114] as implemented in the WANNIER- TOOLS package. Fig. 10(a)–(f) displays the evolution of the Wannier charge centers (WCCs) across the six time-reversal invariant momentum (TRIM)

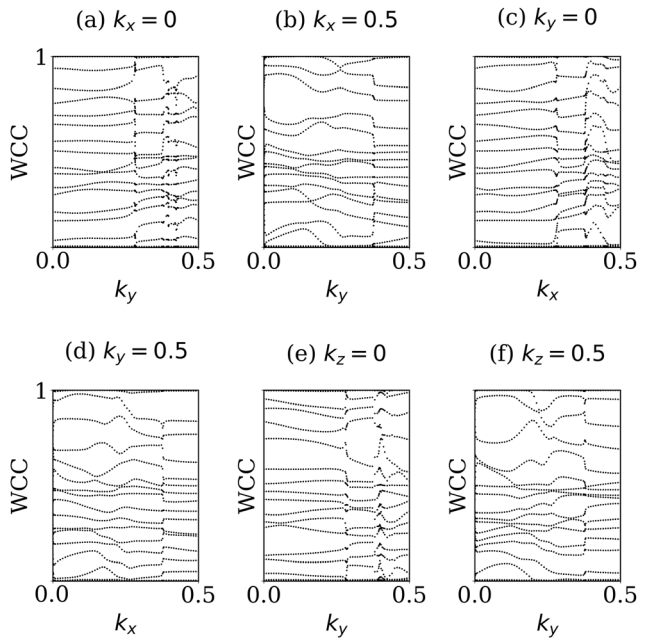

Fig. 10 Evolution of Wannier charge centers (WCCs) on different time-reversal invariant momentum (TRIM) planes.

Table 1 Z_2 topological invariants for six time-reversal invariant momentum (TRIM) planes

Tight-binding	Models plane	Z_2 index
$k_x = 0.0$	k_y–k_z plane	0
$k_x = 0.5$	k_y–k_z plane	1
$k_y = 0.0$	k_x–k_z plane	1
$k_y = 0.5$	k_x–k_z plane	0
$k_z = 0.0$	k_x–k_y plane	1
$k_z = 0.5$	k_x–k_y plane	0

planes. As summarized in Table 1, we observe an odd number of WCC crossings in the $k_x = 0.5$, $k_y = 0.0$, and $k_z = 0.0$ planes, which correspond to nontrivial Z_2 indices. In contrast, the kx = 0.0, ky = 0.5, and $k_z = 0.5$ planes exhibit an even number of crossings, indicating trivial Z_2 indices. From this data, the strong and weak Z_2 indices can be extracted, yielding $(\nu_0; \nu_1\nu_2\nu_3) = (1; 100)$, which indicates that Nd_3In exhibits a strong topological phase. Additionally, employing VASP[115] with vasp2trace and CheckTopologicalMat indicates that Nd_3In is an enforced semimetal with Fermi degeneracy (ESFD), supporting the presence of a nontrivial topological phase.[116] To further elucidate the topological character, we compute the surface states on the (001) surface. These calculations reveal a rich spectrum of topological surface states (TSSs), as illustrated in Fig. 11(a) and (c). The surface-projected band structure along the M–Γ–M direction, shown in Fig. 11(a), exhibits a prominent surface state crossing near the midpoint of Γ–M, within the energy window of 0.10–0.25 eV. This feature corresponds to the bulk type-I Weyl point observed along the Γ–M path. As discussed previously, the inclusion of SOC lifts some of the Weyl nodes and modifies the bulk band structure. Although partial gaps appear, no full insulating gap opens across the Brillouin zone. Consequently, Nd_3In retains its semimetallic character, and the corresponding surface states remain topologically nontrivial, as evidenced by a distinct linear crossing that connects the valence and conduction bands within the partially gapped region. This bridge is highlighted in the magnified inset of Fig. 11(a), underscoring the topological origin of the surface state. The existence of Weyl points in the bulk leads to topologically protected surface states called Fermi arcs that connect projections of Weyl points with opposite chirality.[117] As shown in Fig. 11(b), the Fermi arcs clearly connect the projected Weyl points, thereby confirming the topologically nontrivial nature of the material. We have also investigated the surface states along the M–X–M high-symmetry direction, as illustrated in Fig. 11(c). Notably, around the X point, Rashba splitting occurs near 0.30 eV, where the initially degenerate topological surface states (TSSs) split into two distinct branches.[76] A similar feature is evident along the Γ–M–Γ path near −0.75 eV, highlighting the presence of Rashba-like TSSs that are of considerable interest in spintronics.[118,119]

Before concluding, we briefly discuss the compositional variant In_3Nd, with the corresponding results summarized in SI Materials.[99] The thermodynamic stability of both In_3Nd and Nd_3In was evaluated by constructing the convex hull of the Nd–In system as shown in Fig. S5 of SI Materials. In_3Nd crystallizes in

Open Access Article. Published on 21 October 2025. Downloaded on 12/23/2025 3:16:47 AM.
This article is licensed under a Creative Commons Attribution-NonCommercial 3.0 Unported Licence.

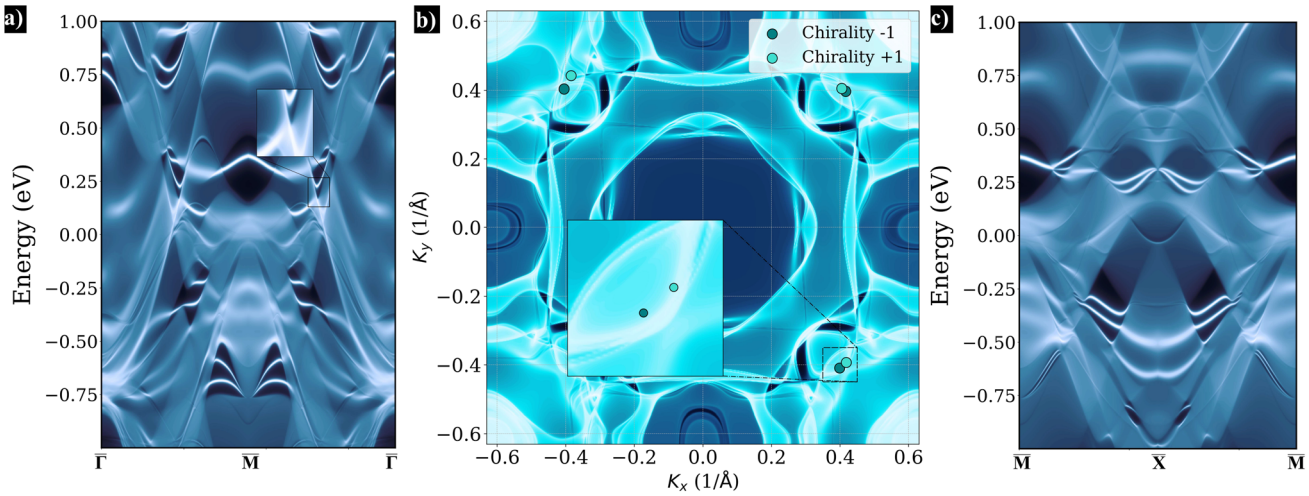

Fig. 11 Surface states obtained using the iterative Green's function method based on the Wannierized Hamiltonian. The intensity scale progresses from black, representing low magnitudes, to light bluish-white, indicating high magnitudes. (a) Simulated angular-resolved photoemission spectroscopy (ARPES) spectrum along the Γ–M–Γ path near the Fermi level. (b) Presence of a Fermi arc verifying the semimetallic behavior. The magnified view highlights the arc connecting Weyl points of opposite chirality. (c) Topological surface states (TSSs) along the M–X–M path.

the AuCu3-type structure with a lattice constant of 4.721 Å without SOC (4.684 Å with SOC). We find that this material also exhibits semimetallic superconductivity. Orbital-projected band structures and projected density of states without and with SOC are shown in Fig. S6 and S7, respectively. Fig. S5 reveals several type-I Weyl points that are gapped out upon inclusion of SOC, resulting in a continuous gap between the highest valence band and the lowest conduction band. Notably, a Weyl point is observed precisely at the Fermi level along the M –Γ path. The semimetallic nature of In_3Nd is further supported by the presence of Fermi arcs, as illustrated in Fig. S8. From the superconducting perspective, In_3Nd exhibits a low transition temperature of $T_c = 0.72$ K, with a superconducting gap of 0.11 meV and an electron–phonon coupling constant $\lambda = 0.435$. This significant decrease in T_c relative to Nd_3In is primarily attributed to a substantial decrease in the total electronic density of states at the Fermi level, which decreases from 6.19 to 1.51 states per eV due to the Nd–In site interchange. The mode-resolved electron–phonon coupling strength, Eliashberg spectral function, and electronic density of states for In_3Nd are detailed in Fig. S8. Interestingly, this valency-exchanged phenomenon is also observed in the La–In system, where both La_3In and In_3La crystallize in the AuCu3-type structure. While La_3In is a conventional superconductor,[120] its compositional counterpart In_3La exhibits semimetallic superconductivity.[121,122]

The predictions made in this study offer clear pathways for experimental validation. ARPES offers direct momentum-resolved detection of topological surface states, while STM and quantum oscillations can spatially resolve these states and reveal signatures of the nontrivial Fermi surface topology.[123–127]

4. Conclusions

In summary, our comprehensive first-principles investigation identifies cubic Nd_3In as an unexplored semimetallic superconductor. Starting from its electronic structure, we find that the density of states (DOS) near the Fermi level is predominantly contributed by Nd d orbitals. These orbitals form a three-band Fermi surface, playing a key role in the superconducting mechanism. The inclusion of spin–orbit coupling (SOC) reveals Kramers degeneracy and a gap opening. Phonon dispersion analysis reveals that low-frequency acoustic modes interact strongly with the electronic states, leading to a significant electron–phonon coupling (EPC) strength driven by pronounced Fermi nesting, consistent with strong-coupling superconductivity. To accurately capture its superconducting behavior, we solve the fully anisotropic Migdal–Eliashberg equations, yielding a superconducting transition temperature of $T_c \approx 14$ K at ambient pressure. Despite the pronounced anisotropy in the EPC, the superconducting gap remains single-band in nature. The computed gap to T_c ratio, $2\Delta_0/k_BT_c$, significantly exceeds the BCS weak-coupling limit, further confirming the strong-coupling character of superconductivity in this material. In addition to its superconducting properties, Nd_3In hosts nontrivial band topology, exhibiting characteristics of a Weyl semimetal. The topological analysis reveals surface Fermi arcs and a strong topological index with Z_2 invariants $(\nu_0; \nu_1\nu_2\nu_3) = (1; 100)$, indicating a strong topological phase. The coexistence of strong-coupling superconductivity and nontrivial band topology makes Nd_3In a promising candidate for applications in quantum transport, topological quantum computing, and quantum information technology.

Conflicts of interest

There are no conflicts to declare.

Data availability

The datasets generated and analysed during this study are not publicly available due to their large file sizes, but are available from the corresponding author upon reasonable request.

© 2025 The Author(s). Published by the Royal Society of Chemistry

Open Access Article. Published on 21 October 2025. Downloaded on 12/23/2025 3:16:47 AM. This article is licensed under a Creative Commons Attribution-NonCommercial 3.0 Unported Licence.

Supplementary information is available. See DOI: https://doi.org/10.1039/d5ra05713b.

References

1 Z. Yan, Z. Wu and W. Huang, *Phys. Rev. Lett.*, 2020, **124**, 257001.
2 Y. Yuan, J. Pan, X. Wang, Y. Fang, C. Song, L. Wang, K. He, X. Ma, H. Zhang, F. Huang, *et al.*, *Nat. Phys.*, 2019, **15**, 1046.
3 T. Meng and L. Balents, *Phys. Rev. B*, 2017, **96**, 019901.
4 Y. Li and F. Haldane, *Phys. Rev. Lett.*, 2018, **120**, 067003.
5 C. Wang, L. Gioia and A. Burkov, *Phys. Rev. Lett.*, 2020, **124**, 096603.
6 A. Veyrat, V. Labracherie, D. L. Bashlakov, F. Caglieris, J. I. Facio, G. Shipunov, T. Charvin, R. Acharya, Y. Naidyuk, R. Giraud, *et al.*, *Nano Lett.*, 2023, **23**, 1229.
7 D. A. Kealhofer, L. Galletti, T. Schumann, A. Suslov and S. Stemmer, *Phys. Rev. X*, 2020, **10**, 011050.
8 H. Wei, S.-P. Chao and V. Aji, *Phys. Rev. B*, 2014, **89**, 014506.
9 C. Huang, B. T. Zhou, H. Zhang, B. Yang, R. Liu, H. Wang, Y. Wan, K. Huang, Z. Liao, E. Zhang, *et al.*, *Nat. Commun.*, 2019, **10**, 2217.
10 W.-H. Dong, Y.-Y. Zhang, Y.-F. Zhang, J.-T. Sun, F. Liu and S. Du, *npj Comput. Mater.*, 2022, **8**, 185.
11 J. J. G. Ripoll, *Quantum Information and Quantum Op- Tics with Superconducting Circuits* (Cambridge Univer- sity Press, 2022).
12 X. Liu and M. C. Hersam, *Nat. Rev. Mater.*, 2019, **4**, 669.
13 M. Sato and Y. Ando, *Rep. Prog. Phys.*, 2017, **80**, 076501.
14 H. Liang, Y. Zeng, L. Liu, J. Pu, H. Luo, Z. Xiong, W. Zhang, Z. Niu, L. Fang and Y. Zou, *Inorg. Chem.*, 2024, **63**, 22227.
15 A. Krasnok, P. Dhakal, A. Fedorov, P. Frigola, M. Kelly and S. Kutsaev, *Applied Physics Reviews*, 2024, **11**, 011302.
16 A. Y. Kitaev, *Phys.-Usp.*, 2001, **44**, 131.
17 C. Nayak, S. H. Simon, A. Stern, M. Freedman and S. Das Sarma, *Rev. Mod. Phys.*, 2008, **80**, 1083.
18 J. D. Sau, R. M. Lutchyn, S. Tewari and S. Das Sarma, *Phys. Rev. Lett.*, 2010, **104**, 040502.
19 M. Freedman, A. Kitaev, M. Larsen and Z. Wang, *Bull. Am. Math. Soc.*, 2003, **40**, 31.
20 F. Tang, S. Ono, X. Wan and H. Watanabe, *Phys. Rev. Lett.*, 2022, **129**, 027001.
21 X. Zhang, H. Wang, J. Liu, M. Zhao and F. Liu, *Phys. Rev. B:Condens. Matter Mater. Phys.*, 2023, **108**, 144101.
22 Y. Kasahara, T. Ohnishi, Y. Mizukami, O. Tanaka, S. Ma, K. Sugii, N. Kurita, H. Tanaka, J. Nasu, Y. Mo- tome, *et al.*, *Nature*, 2018, **559**, 227.
23 A. U. Wolter and C. Hess, *Nat. Phys.*, 2022, **18**, 378.
24 L. Fu and C. Kane, in *APS March Meeting Abstracts*, (2008) pp. V10–001.
25 R. A. Molina and J. Gonzalez, *Phys. Rev. Lett.*, 2018, **120**, 146601.
26 M. Uchida, Y. Nakazawa, S. Nishihaya, K. Akiba, M. Kriener, Y. Kozuka, A. Miyake, Y. Taguchi, M. Tokunaga, N. Nagaosa, *et al.*, *Nat. Commun.*, 2017, **8**, 2274.
27 B. Fu, J.-Y. Zou, Z.-A. Hu, H.-W. Wang and S.-Q. Shen, *npj Quantum Mater.*, 2022, **7**, 94.
28 G. Bednik, A. Zyuzin and A. Burkov, *New J. Phys.*, 2016, **18**, 085002.
29 H.-Z. Lu and S.-Q. Shen, *Front. Phys.*, 2017, **12**, 1.
30 Z. Wang, H. Weng, Q. Wu, X. Dai and Z. Fang, *Phys. Rev. B:Condens. Matter Mater. Phys.*, 2013, **88**, 125427.
31 H.-D. Song, D. Sheng, A.-Q. Wang, J.-G. Li, D.-P. Yu and Z.-M. Liao, *Chin. Phys. B*, 2017, **26**, 037301.
32 A. Sufyan and J. A. Larsson, *ACS Omega*, 2023, **8**, 9607.
33 M. L. Adam and A. A. Bala, *J. Phys.:Condens. Matter*, 2021, **33**, 225502.
34 R. Vocaturo, K. Koepernik, J. I. Facio, C. Timm, I. C. Fulga, O. Janson and J. van den Brink, *Phys. Rev. B*, 2024, **110**, 054504.
35 M. Salis, Y. Huang and A. De Visser, *Phys. Rev. B*, 2021, **103**, 104502.
36 H. Leng, C. Paulsen, Y. Huang and A. De Visser, *Phys. Rev. B:Condens. Matter Mater. Phys.*, 2017, **96**, 220506.
37 B. Rosenstein and B. Y. Shapiro, *2D Materials*, 2023, **10**, 035021.
38 Y. T. Chan, P. Alireza, K. Yip, Q. Niu, K. Lai and S. K. Goh, *Phys. Rev. B*, 2017, **96**, 180504.
39 J. Zhang and G. Huang, *J. Phys.: Condens. Matter*, 2020, **32**, 205702.
40 D. Campi, S. Kumari and N. Marzari, *Nano Lett.*, 2021, **21**, 3435.
41 G. Shenoy, B. Dunlap, G. Kalvius, A. Toxen and R. Gambino, *J. Appl. Phys.*, 1970, **41**, 1317.
42 Y. Du, W. Zhu, X. Nie, D. He, Y. Zhang, P. Wei, W. Zhao and Q. Zhang, *J. Alloys Compd.*, 2025, **1024**, 180239.
43 H. Lu and L. Huang, *Phys. Rev. B*, 2021, **103**, 205134.
44 Z. Yin, X. Du, S. Zhang, C. Chen, D. Pei, J. Zhou, X. Gu, R. Xu, Q. Zhang, W. Zhao, *et al.*, *Phys. Rev. Mater.*, 2022, **6**, 084203.
45 Y. Yang, R. Wang and X. Chen, *Phys. Rev. B*, 2024, **109**, 205103.
46 E. Cheng, W. Xia, X. Shi, Z. Yu, L. Wang, L. Yan, D. C. Peets, C. Zhu, H. Su, Y. Zhang, *et al.*, *npj Quantum Mater.*, 2020, **5**, 38.
47 X. Luo, D. Shao, Q. Pei, J. Song, L. Hu, Y. Han, X. Zhu, W. Song, W. Lu and Y. Sun, *J. Mater. Chem. C*, 2015, **3**, 11432.
48 S. Bagcı, H. Yarar and H. Y. Uzunok, *Ann. Phys.*, 2023, **535**, 2300162.
49 Z. Tu, P. Sun, D. Jia, H. Gou, K. Liu and H. Lei, *Chin. Phys. Lett.*, 2025, **42**, 027302.
50 H. Siddiquee, R. Munir, C. Dissanayake, P. Vaidya, C. Nickle, E. Del Barco, G. Lamura, C. Baines, S. Ca- hen, C. Herold, *et al.*, *Phys. Rev. B*, 2022, **105**, 094508.
51 K. H. Siddiquee, R. Munir, C. Dissanayake, X. Hu, S. Yadav, Y. Takano, E. S. Choi, D. Le, T. S. Rah- man and Y. Nakajima, *J. Phys.: Condens. Matter*, 2021, **33**, 17LT01.
52 K. Kawashima, M. Maruyama, M. Fukuma and J. Akimitsu, *Phys. Rev. B:Condens. Matter Mater. Phys.*, 2010, **82**, 094517.
53 X.-H. Tu, P.-F. Liu and B.-T. Wang, *Phys. Rev. Mater.*, 2019, **3**, 054202.
54 S. Singh and R. Kumar, *J. Supercond. Novel Magn.*, 2019, **32**, 3431.

Open Access Article. Published on 21 October 2025. Downloaded on 12/23/2025 3:16:47 AM. This article is licensed under a Creative Commons Attribution-NonCommercial 3.0 Unported Licence.

55 N. Banno, *Superconductivity*, 2023, **6**, 100047.
56 X. Xu, *Supercond. Sci. Technol.*, 2017, **30**, 093001.
57 S. Posen, M. Liepe, G. Eremeev, U. Pudasaini, and C. Reece, *arXiv Preprint arXiv:2203.06752* (2022).
58 F. Buta, M. Bonura, D. Matera, G. Bovone, A. Ballar- ino, S. Hopkins, B. Bordini, X. Chaud and C. Senatore, *JPhys mater*, 2021, **4**, 025003.
59 Y. Miyoshi, N. Banno, K. Saito, *Superconductors for Fusion: a Roadmap*, 2021, vol. 6, p. 38.
60 Mentink and G. T. Matthias, An experimental and computational study of strain sensitivity in superconducting Nb_3Sn, PhD thesis, University of Twente, 2014.
61 M. Yao, M. Gutierrez-Amigo, S. Roychowdhury, I. Er- rea, A. Fedorov, V. N. Strocov, M. G. Vergniory, and C. Felser, *arXiv Preprint arXiv:2403.03324* (2024).
62 H. Deng, H. Qin, G. Liu, T. Yang, R. Fu, Z. Zhang, X. Wu, Z. Wang, Y. Shi, J. Liu, *et al.*, *Nature*, 2024, **632**, 775.
63 F. Ming, X. Wu, C. Chen, K. D. Wang, P. Mai, T. A. Maier, J. Strockoz, J. Venderbos, C. Gonzaĺez, J. Or- tega, *et al.*, *Nat. Phys.*, 2023, **19**, 500.
64 A. Kuibarov, O. Suvorov, R. Vocaturo, A. Fedorov, R. Lou, L. Merkwitz, V. Voroshnin, J. I. Facio, K. Koepernik, A. Yaresko, *et al.*, *Nature*, 2024, **626**, 294.
65 X. P. Yang, Y. Zhong, S. Mardanya, T. A. Cochran, R. Chapai, A. Mine, J. Zhang, J. Sańchez-Barriga, Z.-J. Cheng, O. J. Clark, *et al.*, *Phys. Rev. Lett.*, 2023, **130**, 046402.
66 J.-T. Zhao, Z.-C. Dong, J. Vaughey, J. E. Ostenson and J. D. Corbett, *J. Alloys Compd.*, 1995, **230**, 1.
67 H. Fukazawa and K. Yamada, *J. Phys. Soc. Jpn.*, 2003, **72**, 2449.
68 M. Merriam, M. Jensen and B. Coles, *Phys. Rev. B:Condens. Matter Mater. Phys.*, 1963, **130**, 1719.
69 M. Merriam and M. Von Herzen, *Phys. Rev. B:Condens. Matter Mater. Phys.*, 1963, **131**, 637.
70 M. Merriam, J. Hagen and H. Luo, *Phys. Rev. B:Condens. Matter Mater. Phys.*, 1967, **154**, 424.
71 T. Stromberg and C. Swenson, *Phys. Rev. B:Condens. Matter Mater. Phys.*, 1964, **134**, A21.
72 A. Jassim and F. Abed, *Journal of Non-Oxide Glasses*, 2019, **11**, 41.
73 A. Biju, P. Sarun, R. Aloysius and U. Syamaprasad, *Mater. Res. Bull.*, 2007, **42**, 2057.
74 P. Cheng, B. Shen, G. Mu, X. Zhu, F. Han, B. Zeng and H.-H. Wen, *Europhys. Lett.*, 2009, **85**, 67003.
75 J. Moriarty, J. Humphreys, R. Gordon and N. Baen- ziger, *Acta Crystallogr.*, 1966, **21**, 840.
76 J. Zhang, K.-Y. Jiang, S.-X. Qiao, P.-C. Xiao, N. Jiao, P. Zhang, H.-Y. Lu and Q.-F. Liang, *Phys. Rev. B*, 2025, **111**, 094508.
77 S. Yatsenko, A. Semyannikov, H. Shakarov and E. Fedorova, *J. Less-Common Met.*, 1983, **90**, 95.
78 P. Giannozzi, S. Baroni, N. Bonini, M. Calandra, R. Car, C. Cavazzoni, D. Ceresoli, G. L. Chiarotti, M. Cococcioni, I. Dabo, *et al.*, *J. Phys.:Condens. Matter*, 2009, **21**, 395502.
79 Y. Gu, S. Zhu, X. Wang, J. Hu and H. Chen, *Commun. Phys.*, 2020, **3**, 84.
80 X. Liu and I. Nlebedim, *AIP Adv.*, 2024, **14**, 015030.
81 S. Ferrari and D. Errandonea, *Crystals*, 2024, **14**, 831.
82 S. Ponće, E. R. Margine, C. Verdi and F. Giustino, *Comput. Phys. Commun.*, 2016, **209**, 116.
83 P. B. Allen and R. Dynes, *Phys. Rev. B*, 1975, **12**, 905.
84 A. A. Mostofi, J. R. Yates, Y.-S. Lee, I. Souza, D. Van- derbilt and N. Marzari, *Comput. Phys. Commun.*, 2008, **178**, 685.
85 Q. Wu, S. Zhang, H.-F. Song, M. Troyer and A. A. Soluyanov, *Comput. Phys. Commun.*, 2018, **224**, 405.
86 A. Yang, X. Tao, Y. Quan and P. Zhang, *Phys. Rev. B:Condens. Matter Mater. Phys.*, 2024, **110**, 174504.
87 J. Chen and Y. Ge, *Phys. Rev. B*, 2021, **103**, 064510.
88 J. Chen and J. Gao, *Phys. Status Solidi RRL*, 2022, **16**, 2100477.
89 B. Wang, H. Gao, Q. Lu, W. Xie, Y. Ge, Y.-H. Zhao, K. Zhang and Y. Liu, *Phys. Rev. B*, 2018, **98**, 115164.
90 A. A. Soluyanov, D. Gresch, Z. Wang, Q. Wu, M. Troyer, X. Dai and B. A. Bernevig, *Nature*, 2015, **527**, 495.
91 C. Wang, Y. Zhang, J. Huang, S. Nie, G. Liu, A. Liang, Y. Zhang, B. Shen, J. Liu, C. Hu, *et al.*, *Phys. Rev. B*, 2016, **94**, 241119.
92 D. Liu, E. Liu, Q. Xu, J. Shen, Y. Li, D. Pei, A. Liang, P. Dudin, T. Kim, C. Cacho, *et al.*, *npj Quantum Mater.*, 2022, **7**, 11.
93 N. Rösch, *Chem. Phys.*, 1983, **80**, 1.
94 N. Karn and V. Awana, *Mater. Today: Proc.*, 2023, S2214785323028174.
95 X.-T. Jin, X.-W. Yan and M. Gao, *Phys. Rev. B*, 2020, **101**, 134518.
96 P. Jamwal, R. Ahuja and R. Kumar, *J. Phys.: Condens. Matter*, 2024, **36**, 385903.
97 S. Patel, S. Jena and A. Taraphder, *Phys. Rev. B*, 2024, **110**, 014507.
98 Y. Sun, F. Zhang, C.-Z. Wang, K.-M. Ho, I. I. Mazin and V. Antropov, *Phys. Rev. Mater.*, 2022, **6**, 074801.
99 See SI Material at [URL] (2025).
100 P.-F. Liu, F. Zheng, J. Li, J.-G. Si, L. Wei, J. Zhang and B.-T. Wang, *Phys. Rev. B*, 2022, **105**, 245420.
101 W. Kohn, *Phys. Rev. Lett.*, 1959, **2**, 393.
102 N. Girotto and D. Novko, *Phys. Rev. B*, 2023, **107**, 064310.
103 J.-N. Wang, X.-W. Yan and M. Gao, *Phys. Rev. B*, 2021, **103**, 144515.
104 Q. Gu, Y. Li, S. Wan, H. Li, W. Guo, H. Yang, Q. Li, X. Zhu, X. Pan, Y. Nie, *et al.*, *Nat. Commun.*, 2020, **11**, 6027.
105 Z. Li and S. G. Louie, *Phys. Rev. Lett.*, 2024, **133**, 126401.
106 S. Pramanick, S. Chakraborty, and A. Taraphder, *arXiv Preprint arXiv:2505.10905* (2025).
107 J.-Y. Chen, S.-L. Fu, C.-A. Wang, Y.-L. Chen, J.-H. Wang, R.-R. Deng, Y.-P. Xie, X.-L. Gao and X.-Q. Wu, *Eur. Phys. J. B*, 2025, **98**, 1.
108 H. Chen, Y. Tang, H. Jiang, X. Jiang, J. Wang, C. Zhang, D. Duan, J. Dong and Y. Ma, *Chin. Phys. Lett.*, 2024, 017402.
109 Y. Zhao, S. Zeng, C. Lian, Z. Dai, S. Meng and J. Ni, *Phys. Rev. B*, 2018, **98**, 134514.
110 H. J. Choi, D. Roundy, H. Sun, M. L. Cohen and S. G. Louie, *Phys. Rev. B*, 2002, **66**, 020513.
111 E. Margine and F. Giustino, *Phys. Rev. B*, 2014, **90**, 014518.

© 2025 The Author(s). Published by the Royal Society of Chemistry

Open Access Article. Published on 21 October 2025. Downloaded on 12/23/2025 3:16:47 AM.
This article is licensed under a Creative Commons Attribution-NonCommercial 3.0 Unported Licence.

112 L. Fu and C. L. Kane, *Phys. Rev. B:Condens. Matter Mater. Phys.*, 2007, **76**, 045302.
113 A. A. Soluyanov and D. Vanderbilt, *Phys. Rev. B:Condens. Matter Mater. Phys.*, 2011, **83**, 235401.
114 R. Yu, X. L. Qi, A. Bernevig, Z. Fang and X. Dai, *Phys. Rev. B:Condens. Matter Mater. Phys.*, 2011, **84**, 075119.
115 G. Kresse and J. Furthmüller, *Phys. Rev. B*, 1996, **54**, 11169.
116 M. Vergniory, L. Elcoro, C. Felser, N. Regnault, B. A. Bernevig and Z. Wang, *Nature*, 2019, **566**, 480.
117 S. S. Nourizadeh, A. Vaez, and D. Vashaee, *Advanced Quantum Technologies*, vol. 6, p. 2300072 2023.
118 G. Bihlmayer, P. Nöel, D. V. Vyalikh, E. V. Chulkov and A. Manchon, *Nat. Rev. Phys.*, 2022, **4**, 642.
119 K. Ishizaka, M. Bahramy, H. Murakawa, M. Sakano, T. Shimojima, T. Sonobe, K. Koizumi, S. Shin, H. Miyahara, A. Kimura, *et al.*, *Nat. Mater.*, 2011, **10**, 521.
120 E. Sampathkumaran, *Solid State Commun.*, 2014, **181**, 54.
121 Y. Wan, C. Cheng, X. He and J. Chang, *J. Superhard Mater.*, 2021, **43**, 31.
122 S. M. Teicher, J. F. Linnartz, R. Singha, D. Pizzirani, S. Klemenz, S. Wiedmann, J. Cano and L. M. Schoop, *Chem. Mater.*, 2022, **34**, 4446.
123 H. Yang, M. Schmidt, V. Süss, M. Chan, F. F. Bal- akirev, R. D. McDonald, S. S. Parkin, C. Felser, B. Yan and P. J. Moll, *New J. Phys.*, 2018, **20**, 043008.
124 A. Soumyanarayanan and J. E. Hoffman, *J. Electron Spectrosc. Relat. Phenom.*, 2015, **201**, 66.
125 K. Shrestha, R. Chapai, B. K. Pokharel, D. Miertschin, T. Nguyen, X. Zhou, D. Chung, M. Kanatzidis, J. Mitchell, U. Welp, *et al.*, *Phys. Rev. B*, 2022, **105**, 024508.
126 B. Lv, T. Qian and H. Ding, *Rev. Mod. Phys.*, 2021, **93**, 025002.
127 B. Ghosh, D. Mondal, C.-N. Kuo, C. S. Lue, J. Nayak, J. Fujii, I. Vobornik, A. Politano and A. Agarwal, *Phys. Rev. B:Condens. Matter Mater. Phys.*, 2019, **100**, 195134.

© 2025 The Author(s). Published by the Royal Society of Chemistry